ARTICLE

Nanomembrane on Graphene: Delamination Dynamics and 3D Construction

Yue Wu, Xinyuan Zhang, Zhe Ma, Weida Hong, Chunyu You, Hong Zhu, Yang Zong, Yuhang Hu, Borui Xu, Gaoshan Huang, Zengfeng Di, and Yongfeng Mei*

Cite This: ACS Nano 2025, 19, 331−344

Read Online

ACCESS | 📊 Metrics & More | 📄 Article Recommendations | 🔵 Supporting Information

ABSTRACT: Freestanding nanomembranes fabricated by lift-off technology have been widely utilized in microelectromechanical systems, soft electronics, and microrobotics. However, a conventional chemical etching strategy to eliminate nanomembrane adhesion often restricts material choice and compromises quality. Herein, we propose a nanomembrane-on-graphene strategy that leverages the weak van der Waals adhesion on graphene to achieve scalable and controllable release and 3D construction of nanomembranes. This fragile adhesion allows for precise delamination under stimulations, such as surface tension, thermal treatment, and mechanical bending. This strategy is compatible with various inorganic materials, including oxides, semiconductors, and metals, and allows for precise control of rolling and folding into 3D microstructures. Demonstrations include tubular microrobots with diverse locomotion and biodegradable nerve scaffolds based on facile delamination. Our nanomembrane-on-graphene strategy offers a versatile platform for the fabrication of functionalized microstructures.

KEYWORDS: graphene, nanomembrane, adhesion, origami, folding, three-dimensional microstructure
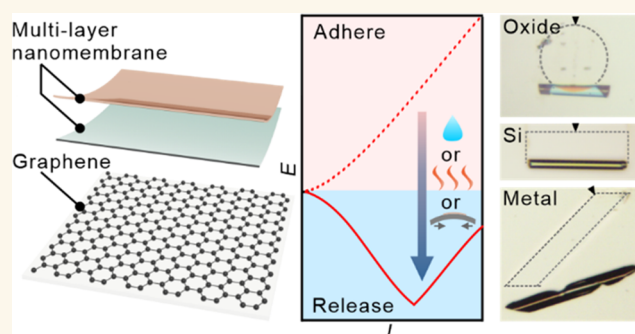
With the continuous miniaturization of micro- and nanostructured objects and devices, adhesion turns up to be a fundamental issue both in the fabrication and function.[1−3] The adhesion between layers and the substrate plays a vital role in microelectromechanical systems (MEMSs),[4−7] soft electronics,[8−11] and microrobotics[12−14] due to the requirement of freestanding nanomembranes. Therefore, a lift-off process is always applied to break the initial adhesion between the nanomembranes and their underlying substrates. Conventional MEMS fabrication involves a surface micromachining strategy, where a lift-off step is achieved by depositing nanomembranes onto a sacrificial layer, which is then selectively etched away to release the structures.[15] However, this etching process requires the matching between the sacrificial layer and the preserved nanomembrane[16] and thus constrains the versatility of fabrication and can compromise the quality of the freestanding nanomembranes. To address this, polymer-based sacrificial layers were later introduced to reduce adhesion and enable the release of freestanding nanomembranes from a broader range of materials. Yet, polymers cannot withstand high-temperature deposition processes, thus further limiting their applicability.[17,18] Therefore, a general release strategy that allows for controlled delamination of versatile materials is desired to obtain high-quality freestanding nanomembranes and their corresponding constructed 3D structures.[19,20]

On the other hand, very weak adhesion may lead to spontaneous nanomembrane (i.e., thin films) delamination and buckling from the substrate in the first place,[21,22] which is a common failure during the MEMS fabrication process. This phenomenon inspires advanced methodologies to lift off nanomembranes via altering the adhesion between the substrate and deposited nanomembranes. After the nanomembrane was deposited on designed substrates, 3D microstructures of different materials and their combinations were manufactured from liquid-triggered delamination of nanomembranes.[23−25] This method designed a prelayer to create van der Waals bonding between the nanomembrane and the substrate, for example, metal nanomembranes on oxide substrates, which was broken by liquid intercalation, inducing
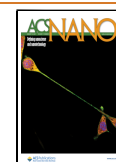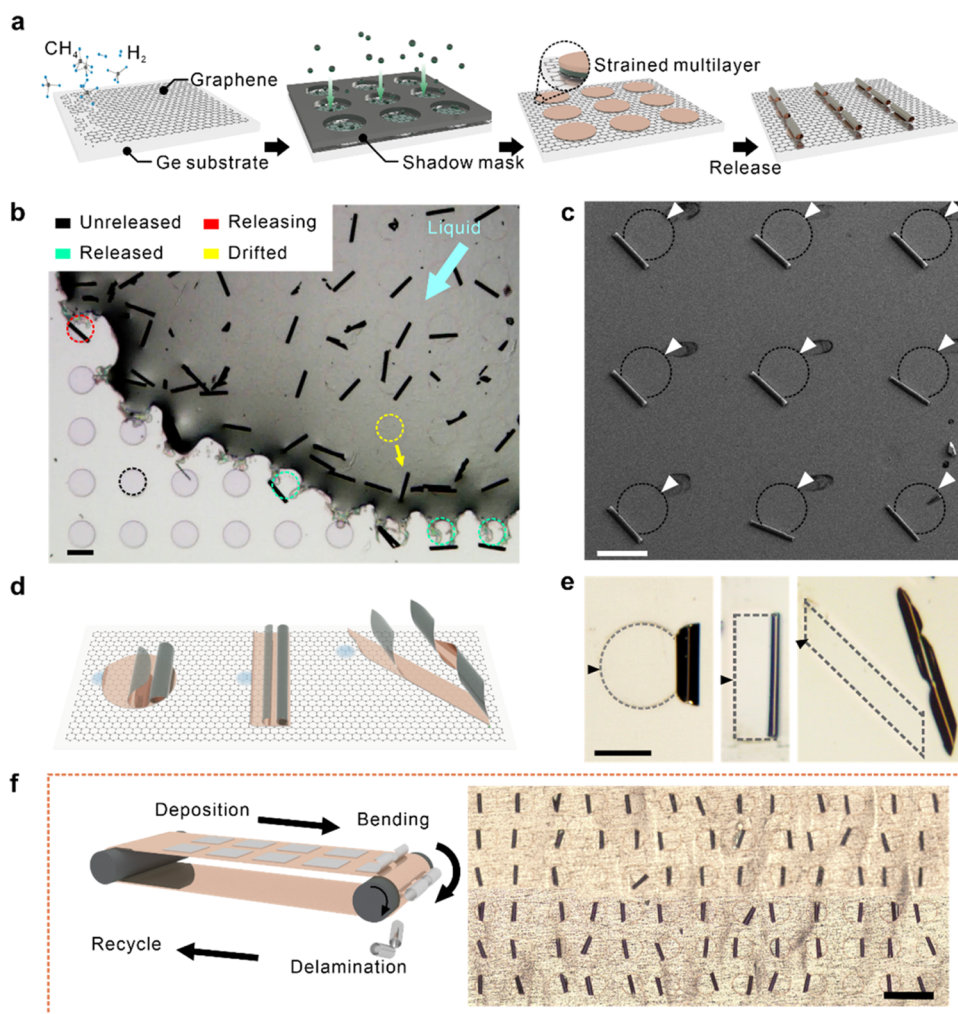
Figure 1. Fabrication of 3D rolling origami by the nanomembrane-on-graphene strategy. (a) Conceptual illustration of a multilayered nanomembrane deposited onto graphene and rolling up after its release. (b) Optical microscopy image of the releasing process of SiO/Cr nanomembranes. Scale bar, 100 μm. (c) SEM image of a 3 × 3 array of SiO/Cr microtubes constructed by individual release triggered by microdroplets. White arrowheads mark the trigger points by microdroplets. Scale bar, 100 μm. (d) Schematic of the microdroplet-triggered individual release of various patterned nanomembranes. (e) Optical microscopy images of rolling origami structures constructed by nanomembranes with different patterns corresponding to the schematics in (d). Black arrowheads mark the trigger points by microdroplets. Scale bar, 100 μm. (f) Conceptual illustration of the roll-to-roll fabrication strategy and an optical microscopy image of a 6 × 13 Si/Ti/Ni microtube array fabricated by the roll-to-roll strategy. The length of the microtubes is 200 μm. Scale bar, 500 μm.

a lift-off of the nanomembrane from the substrate. However, this strategy requires certain material pairing to create weak van der Waals bonding between them, which constrains the number of desirable materials and integration of different microstructures for complicated application scenes.

As the most typical 2D material, graphene has no dangling bonds on the surface, and its adhesion with upper layers is therefore dominated by weak van der Waals force.[26−28] Thus, graphene is considered to be able to serve as an ideal substrate for nanomembrane delamination and transfer processes.[29,30] Notably, this interaction principle is suitable for all classes of materials, suggesting the potential of graphene as a general substrate for constructing microstructures from versatile materials. Here, we developed a nanomembrane-on-graphene strategy that adopts graphene as the substrate to facilitate delamination of nanomembranes. We demonstrated that by applying external stimulations, the weak van der Waals interactions can be overcome, causing nanomembranes on the graphene substrate to delaminate and spontaneously roll

into tubular or helical structures due to the built-in strain gradient. The underlying mechanism of this facile delamination process is further elucidated through quantitative energy analysis. With predesigned patterns, tunable deposition parameters, and controllable rolling directions, the 3D microstructures of metal, semiconductor, and oxide with sophisticated designs can be precisely predicted and constructed. By utilizing the proposed approach, tubular microrobots that can be assembled into different patterns as well as biodegradable and conductive nerve scaffolds are demonstrated. This nanomembrane-on-graphene strategy provides a general platform for constructing 3D microstructures with versatile materials and geometries to meet complicated application demands.

RESULTS AND DISCUSSION

Rolling Origami on the Graphene Substrate. The conceptual image of 3D microstructure fabrication using a nanomembrane-on-graphene strategy is shown in Figure 1a.
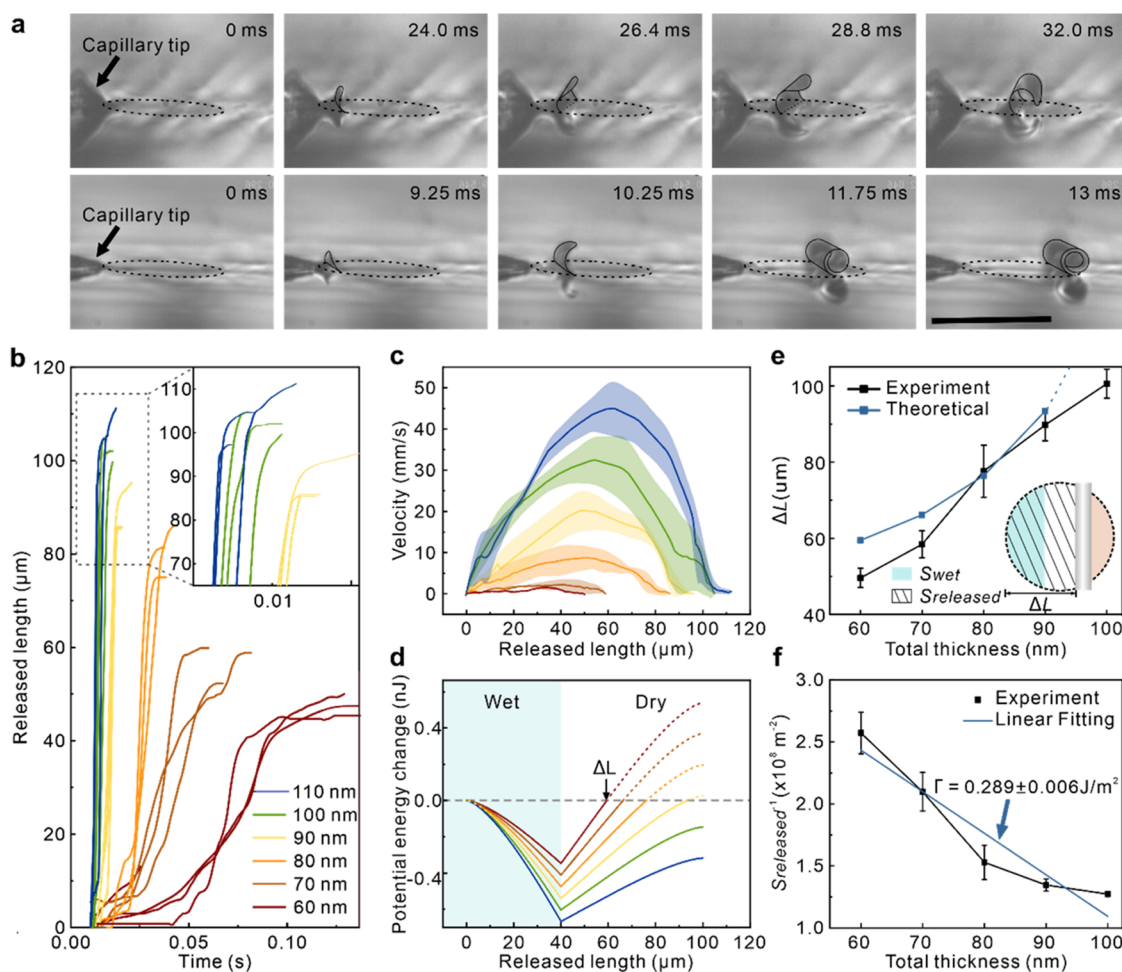
Figure 2. Microdroplet-triggered delamination on a graphene substrate. (a) Side view of the nanomembrane after liquid treatment according to time evolution. The thickness of the SiO/Cr nanomembrane is 40/40 nm for the first row and 45/45 nm for the second. Scale bar, 100 μm. (b) Released length according to time evolution for nanomembranes with different total thicknesses. The inset shows a magnified view of the region with an extremely short delamination time. (c) Releasing velocity as a function of released length for nanomembranes with different total thicknesses. The solid line is the average releasing velocity and the shaded region represents the standard deviation. (d) Calculated potential energy change during delamination after ethanol treatment for nanomembranes with different thicknesses. The solid line marks successful delamination, while the dashed line indicates the prohibited delamination state. (e) Relation between the final released distance ΔL and the total thickness. The inset illustrates the definition of ΔL, area of the wetted region S_{wet}, and released area $S_{released}$. (f) Relation between the released area $S_{released}$ and the total thickness.

First, monolayer graphene was grown on a Ge wafer by chemical vapor deposition (CVD). Raman spectra in Figure S1 depict clear G and 2D bands with an intensity ratio larger than 1.5, which confirms the monolayer feature of graphene.[31] Next, a shadow mask was applied to define the target region for nanomembrane deposition. Multilayers were then deposited on the graphene substrate using e-beam evaporation, where differences in thermal expansion coefficients and deposition parameters between the layers led to the generation of strain gradients within the nanomembrane. After deposition, the shadow mask was removed. By applying an external stimulation, such as liquid intercalation, mechanical bending, and thermal treatment (Figure S2), the nanomembrane was delaminated from the graphene substrate and rolled up into tubular 3D microstructures under an internal strain gradient generated during deposition. We also conducted Raman characterization of the substrate after delamination, which confirmed that the graphene remained on the Ge substrate after the delamination process (Figure S1). Massive production of dozens of microtubes was achieved by simply

dipping one drop of ethanol onto a sample with an array of circular SiO/Cr nanomembranes (Figure 1b). Here, the Cr layer is deposited to generate a strain gradient that causes the corresponding nanomembranes to roll up. When the liquid droplet flows on the graphene substrate toward the lower-left corner, nanomembranes are released sequentially, and microstructures under different release stages are marked by four colored circles. The black circle marks an as-deposited nanomembrane untouched by the ethanol liquid, and its plane geometry indicates firm adhesion to the substrate. As the boundary of the droplet reaches the rim of each nanomembrane, the contact point bends upward and scrolls in a direction parallel to the liquid flow (red circle). Then, the remaining part continues to roll up until it reaches the opposite edge of the nanomembrane, forming a tubular microstructure (green circle). Sunk in the ethanol droplet, the microtube finally delaminates completely and may drift away with the liquid flow (yellow circle). From the ethanol trace around and under the patterned area, it can be deduced that the liquid intercalates between the nanomembrane and the graphene

substrate, leading to initial delamination of the fringe of the nanomembrane, which further delaminates under a built-in strain.

Nanomembranes may also be triggered individually by microdroplets to form a uniformly arranged array of microtubes on graphene (Figure 1c). The microdroplet is produced by a glass capillary containing ethanol, which was secured to a micromanipulator. As the tip contacts the surface of graphene, the microdroplet is ejected onto the surface under capillary force and surface tension, triggering the edge of the nanomembrane at the contact point (marked by white arrows) to delaminate from graphene. With the triggering points of same positions, the nanomembranes roll approximately in the same direction into parallel microtubes. The morphology of rolling origami can be tuned by applying shadow masks with different shapes, as sketched in Figure 1d and demonstrated by the experimental results in Figure 1e. The circular nanomembranes form microtubes with arched edges and the rectangular ones with smooth edges, while the nanomembranes with parallelogram shapes form helical structures. Moreover, the released microstructures can be easily transferred onto a new substrate (Figure S3). Rolled-up microstructures are reinforced with a 50 nm thick Al_2O_3 coating, and then the PVA solution is dipped and dried, forming a solid film on the released microstructures as a protective coating. The PVA film including Al_2O_3 coating is then peeled off from the substrate and is transferred onto the target substrate, and PVA is dissolved in water. Similarly, the strained nanomembranes can be peeled off from graphene and transferred onto the target substrate first and then released to construct microtubes (Figure S4). The transfer technique offers a greater degree of flexibility in designing the functional device on desired substrates.

In addition to liquid-triggered delamination, we demonstrated a roll-to-roll fabrication strategy that does not necessarily require the involvement of liquid or vapor and is more suitable for future practice in flowline production (Figure 1f). Graphene on copper foil was utilized for its flexibility, and an array of multilayer nanomembranes was deposited onto the substrate. As the specimen was wound around the roller, the nanomembranes spontaneously detached from the substrate and rolled up into 3D tubular microstructures, and this phenomenon is attributed to the additional internal strain gradient generated by the bending moment. Here, a 6 × 13 array of microtubes of Si/Ti/Ni nanomembranes was obtained (Figure 1f), demonstrating the feasibility of the approach. It can be noticed that the rolling directions of most microtubes are consistent and are perpendicular to the bending direction of copper foil (73 out of 76 microtubes), as the delamination tends to happen alone in the direction with the quickest energy release rate. The missing nanomembranes indicate fully delaminated microtubes that are detached from the surface. A larger array of 35 × 20 microtubes was also demonstrated, and the yield was estimated to be 83% (Figure S5). This facile release process is rapid, avoids contamination from liquids, and allows a controllable releasing direction. The advantage of the roll-to-roll release strategy is its feasibility in the industrialized massive production of functionalized microstructures. Furthermore, we conducted experiments to recycle the graphene substrate after nanomembrane deposition and release (Figure S6), aiming to reduce the cost of graphene for real-world applications.

Dynamics of Liquid-Triggered Delamination. In order to provide an insight into the mechanism of facile delamination on graphene, the interaction between the fundamental graphene−nanomembrane interface and the internal strain gradient in nanomembranes should be clarified first. Experimentally, a series of SiO/Cr nanomembranes with altered thickness ranging from 30/30 to 55/55 nm were prepared, and a high-speed camera was utilized to record the dynamic delamination process from the side (see the details of the experimental setup in Figure S7). Here, circular patterns were chosen to eliminate the effect of geometric asymmetry. Images of the morphology changes of 40/40 and 45/45 nm nanomembranes extracted from a high-speed video are shown in Figure 2a. When the microcapillary was in contact with the rim of the nanomembrane from the left side, ethanol intercalated into the nanomembrane−substrate interface and peeled the edge of the nanomembrane off from the substrate, which is a relatively slow process (second column). As the microdroplet advanced, the released area expanded and the freestanding part bent into a tubular geometry (third column), which rolled forward. The rolling of the nanomembrane in turn induced further delamination, and the nanomembrane detached from the region near the microcapillary, which is wetted by the ethanol microdroplet (third to fourth columns). The delamination continued for a few microseconds until it finally terminated at the right side of the nanomembrane (fifth column). Here, the distance between the contacting point and the boundary of the fixed nanomembrane is defined as the released length, and the released length after the whole delamination process (i.e., the final stable status) is labeled as the final released distance ΔL. In Figure 2b, we analyzed the released length according to the time evolution from each frame of the recorded video to further examine the dynamic delamination process. For each thickness, three nanomembranes were evaluated, and the curves were marked with different colors for different thicknesses. The delamination processes for all nanomembranes show a similar motion fashion, but for thicker nanomembranes the delamination time reduced sharply and ΔL increased. The average releasing velocity was calculated as a function of the released length for varied nanomembrane thicknesses, as is sketched in Figure 2c, which exhibits two delamination stages. In the first stage, the microdroplet triggered the intercalation, and the releasing velocity accelerated with the length. After the nanomembrane was disengaged from the wetted region, it shifted to the second stage, and the nanomembrane continued to roll forward under the influence of the built-in strain gradient and inertia until its velocity gradually approached zero. It is noted that the releasing velocity of the thicker nanomembrane is higher than that of the thinner one, with the peak velocity as high as 45.27 mm/s (55/55 nm nanomembrane), which is around 10 times faster than that of the 30/30 nm nanomembrane.

To investigate the underlying mechanism that influences the dynamic delamination process, the corresponding energy variation of the system was examined. The total energy of the system should be composed of the interface energy change between the nanomembrane and graphene (ΔU_s), the elastic strain energy stored in the as-deposited nanomembrane (ΔU_E), and kinetic energy of the rolling motion (K). Adding up all these elements and assuming energy conservation gives

$$\Delta U_E + \Delta U_s + K = 0 \tag{1}$$
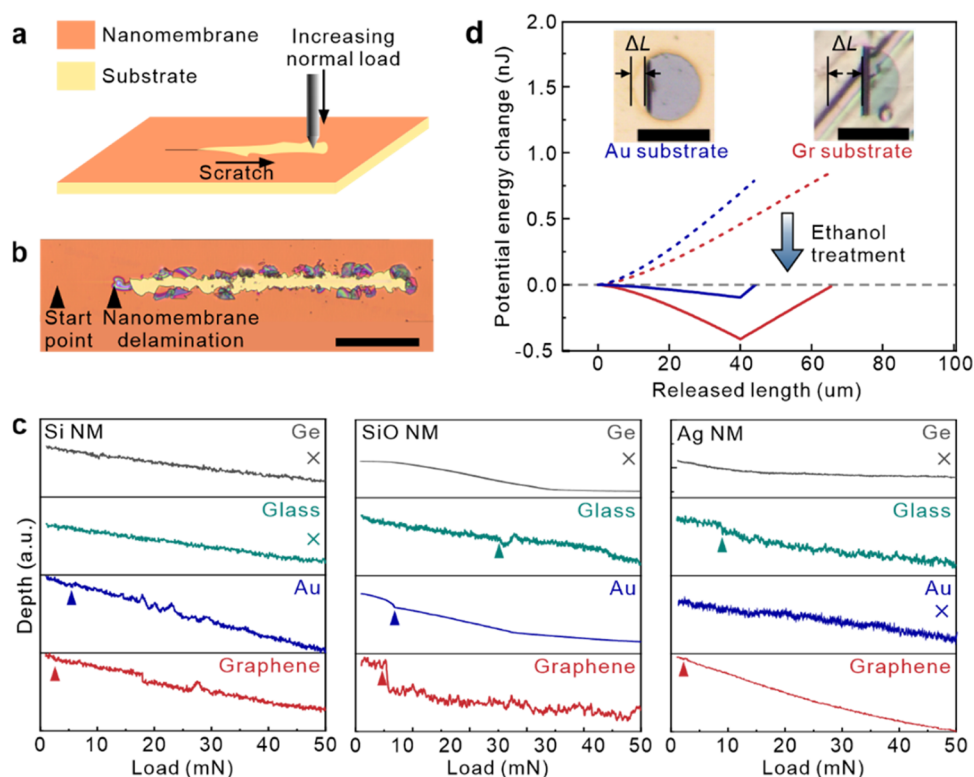
Figure 3. Comparison of nanomembrane adhesion and delamination behaviors on graphene and other substrates. (a) Schematic illustration of the nanoindentation test. (b) Optical image of a scratch during the nanoindentation test. Black arrows mark the point where the scratch starts and the critical point where the nanomembrane delaminates. Scale bar, 100 μm. (c) Nanoindentation test of Si, SiO, and Ag nanomembranes on graphene, Au, glass, and Ge substrates. Arrows point the critical load when the scratching depth display a sudden change, indicating delamination of the nanomembrane. (d) Calculated potential energy change during delamination with (solid line) and without (dashed line) ethanol treatment for 35/35 nm SiO/Cr nanomembranes on Au and graphene substrates. Blue lines correspond to nanomembranes on the Au substrate and red lines represent nanomembranes on the graphene substrate. Insets show the optical microscopy images of the corresponding nanomembranes triggered on Au and graphene substrates with different final released distances (ΔL). Scale bar, 100 μm.

where ΔU_E and ΔU_s constitute the potential energy change (ΔU_P) of the system, which is defined by the equation:

$$\Delta U_P = \Delta U_E + \Delta U_s = -K \qquad (2)$$

As all nanomembranes for energy analysis are composed of same materials with similar deposition parameters, the elastic strain energy ΔU_E relaxed per unit area as the nanomembrane transformed from planar to rolled-up geometry increases proportionally to thickness (Note S1)

$$\Delta U_E = -\Delta V t S_{released} \qquad (3)$$

where ΔV is the elastic strain energy change per unit area of the 1/1 nm nanomembrane, t is the thickness, and $S_{released}$ is the total released area of the nanomembrane. The interface energy change ΔU_s originates from a thermodynamic (reversible) energy cost to create new surfaces, named the Dupré energy of adhesion (hereafter simplified as adhesion energy).[32] We analyzed the theoretical elastic strain energy change of nanomembranes after complete delamination and their corresponding peak velocity with altered thickness (Figure S8a), which confirms that the elastic strain energy change increases with nanomembrane thickness, leading to a quicker velocity. We also calculated the dependence of elastic strain energy change on SiO thickness for the fully delaminated nanomembrane (circle pattern, 100 μm) with a fixed Cr thickness (40 nm), and the results in Figure S8b indicate that

the elastic strain energy change increases with the SiO thickness.

As liquid intercalation only affects part of the delaminated region, the interface energy is divided into two parts:

$$\Delta U_s = \Gamma_{wet} S_{wet} + \Gamma(S_{released} - S_{wet}) \qquad (4)$$

where Γ_{wet} is the wet adhesion energy per unit area of graphene after ethanol intercalation and S_{wet} is the area with wet adhesion, while Γ is the initial dry adhesion energy per unit area between the graphene and the nanomembrane. According to previous studies, we, respectively, set the dry adhesion (Γ) and wet adhesion (Γ_{wet}) between graphene and SiO as 0.31 and 0.013 J m^{-2},[33,34] and the theoretical potential energy changes (ΔU_P) according to the released length for nanomembranes with varied thicknesses before and after ethanol treatment are calculated and demonstrated in Figures S9 and 2d, respectively. From a fracture mechanics perspective, a positive slope of the energy curve indicates prohibited or decelerated motion, while a negative slope represents initiation or acceleration of delamination (Note S2). After ethanol intercalation, the energy curve within the wetted region declines due to reduced adhesion energy and increases again after the nanomembrane detaches from the wetted region, which corroborates the velocity result in Figure 2c. From the energy curve, it can be deduced that more potential energy is released for thicker nanomembranes, which transformed into
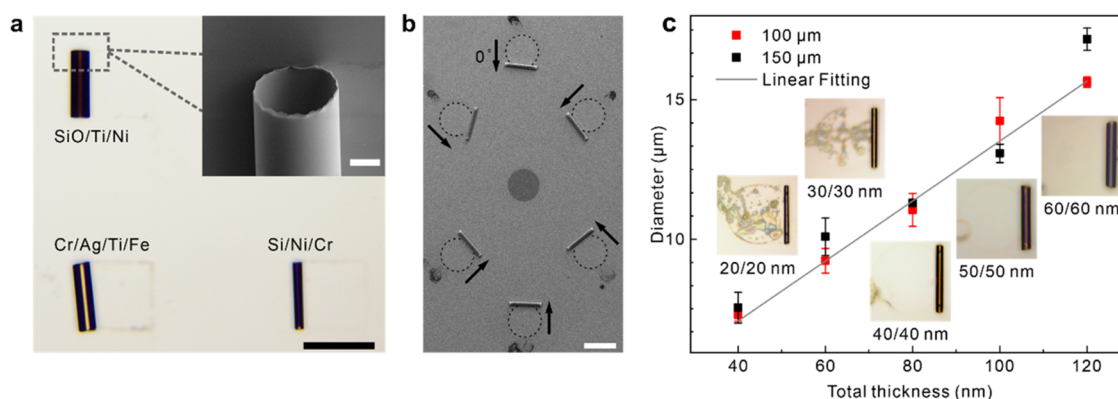
Figure 4. Precise control of configurations of rolled-up microstructures on graphene. (a) Optical microscopy image of SiO/Ti/Ni, Cr/Ag/Ti/Fe, and Si/Ni/Cr microtubes on the same piece of graphene. Scale bar, 100 μm. Inset: SEM image of one end of the SiO/Ti/Ni microtube. Scale bar, 10 μm. (b) Microtubes of different rolling directions from arrays of circular nanomembranes triggered at different points. Black arrows mark the rolling directions. Scale bar, 100 μm. (c) Rolling diameters of microtubes from circular patterns with diameters of 100 μm (red squares) and 150 μm (black squares) as a function of the total thickness of graphene. Insets show the optical microscopy images of a series of microtubes triggered from circular nanomembranes with a diameter of 100 μm.

more kinetic energy, resulting in faster and further delamination. The system reaches a stationary state at the end of the delamination process, and the point where the potential energy change reaches zero marks the theoretical final released distance. Since the kinetic energy K must remain positive, states where ΔU_p is above zero are prohibited, which are marked by dashed lines in Figure 2d. For experimental results, five microtubes are measured for each group, and the relationship between the total thickness and ΔL is depicted in Figure 2e, indicating that ΔL increases with nanomembrane thickness. As the thickness exceeds 50/50 nm, nanomembranes delaminate completely from the substrate and constructed microtubes. The experimental results slightly deviate from the calculated results due to deviations of adhesion energy per unit area Γ between the set value and actual situation, as graphene's surface state is significantly affected by numerous factors such as the fabrication technique, substrate material,[35] surface roughness,[36] and the interface confinement condition.[37]

When the delamination process finally terminates, the kinetic energy returns to zero, and an equation is obtained by substituting eqs 3 and 4 into eq 1:

$$-\Delta V t S_{released} + \Gamma_{wet} S_{wet} + \Gamma(S_{released} - S_{wet}) = 0 \qquad (5)$$

which can be rewritten into the following form

$$\frac{1}{S_{released}} = \frac{\Gamma}{S_{wet}(\Gamma - \Gamma_{wet})} - \frac{\Delta V}{S_{wet}(\Gamma - \Gamma_{wet})} t \qquad (6)$$

It can be deduced from eq 6 that there exists a linear relationship between the reciprocal of the final released area and thickness. As a result, the final released area is calculated by utilizing ΔL and a linear fitting is applied (Figure 2f). Moreover, the practical dry adhesion energy per unit area Γ of graphene and SiO of our experiment can be extracted from the linear fitting parameters as 0.289 ± 0.006 J m^{-2}, which agrees well with the value reported in previous studies,[38,39] indicating a novel strategy for measuring the adhesion energy. It can also be deduced that the mechanism of roll-to-roll release strategy lies in the low energy required to overcome the adhesion between the nanomembrane and graphene substrate, which is easily achieved by external excitations such as bending in this case. Additionally, thermally triggered release is also success-

fully verified, attributed to the additional internal strain gradient generated by mismatch of the thermal expansion coefficients (Figure S10), which also foresees potential for other etching-free release methods, such as those triggered by surface tension[40] and electron beam irradiation.[41] Through the above energy analysis, we set up a theory on the fundamental relation among the elastic strain energy, adhesion, and nanomembrane delamination dynamics, which provides a reasonable explanation for the process of liquid-triggered nanomembrane delamination.

Weak Adhesion of Nanomembranes on Graphene. The energy analysis highlights the influence of adhesive interaction between nanomembranes and their underlying substrate on successful delamination. As a result, the novel adhesive property of graphene may lead to facile nanomembrane delamination and microstructure fabrication for versatile materials. A nanoindentation test was conducted to compare the adhesion of graphene to Au, glass (commonly employed in previous studies[23,24]), and bare germanium substrates. The schematic of the nanoindentation test is shown in Figure 3a. During the test, a normal load is applied to the indentation tip as it moves across the nanomembrane, creating a scratch on the surface. As the load is increased, the scratching depth increases proportionally until the loading force reaches a critical point where the depth undergoes a sudden change, indicating delamination of the nanomembrane from the substrate. This delamination is also visible in optical microscopy images (Figure 3b). Si, SiO, and Ag nanomembranes, which represent semiconductor, oxide, and metal materials, respectively, were tested on the four substrates, with results depicted in Figure 3c, and the corresponding optical images in Figure S11. The critical loads required for the delamination of all three materials from graphene are very low (less than 10 mN), highlighting the universal weak adhesion mechanism of graphene. In contrast, SiO nanomembrane failed to delaminate from the glass substrate, nor did Ag from the Au substrate, and no delamination was observed for any material on the Ge substrate, highlighting the specific role of graphene. Here, the lower adhesion of graphene originated from its low surface energy, as it possessed no dangling bonds on its surface.[42,43] As a result, the adhesion was dominated by weak van der Waals
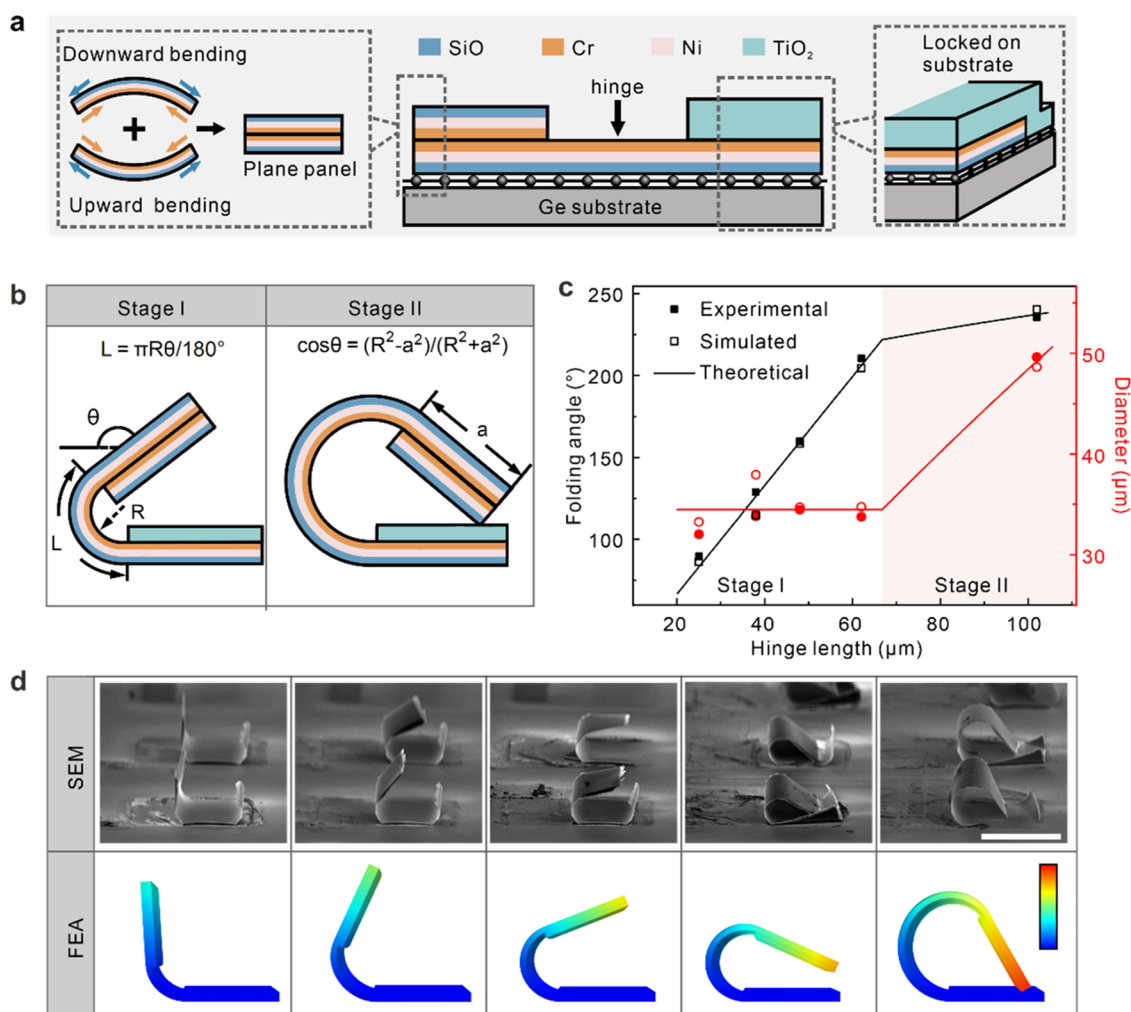
Figure 5. Self-folding on the graphene substrate. (a) Illustration of the designing concept of the folding structure. (b) Cross-section images of folding structures at two different stages. (c) Experimental, calculated, and simulated results of the folding angle θ and curvature diameter R as a function of hinge length L. (d) SEM images of triggered folding structures with different L values and the corresponding simulated results obtained by FEM. Scale bar: 100 μm.

interaction, and this mechanism is generic for all kinds of inorganic materials. For instance, multilayered nanomembranes of SiO/Cr, Si/Cr, and Ag/Cr deposited on the graphene substrate are successfully released to roll up into microtubes (Figure S12). For comparison, Si nanomembranes failed to release on glass and germanium substrates, and Ag remained intact on the Au substrate, which are comparable to the indentation results (Figure S13). In addition to microtubes of pure metal and hybrid materials, pure oxide structures were also available by this method, as exemplified in Figure S14, which depicts two microtubes consisting of SiO/SiO$_2$ and Y$_2$O$_3$/ZrO$_2$. Also, the energy analysis approach was conducted to compare the delamination manner on graphene and Au substrates. 35/35 nm SiO/Cr nanomembranes were deposited and triggered on two kinds of substrates, and the potential energy change of the system as a function of released length was calculated (Figure 3d). Without ethanol treatment, the potential energy change for both substrates remained above zero, indicating prohibited delamination (red and blue dashed lines). The adhesion energy per unit area for SiO/Au was 0.39 J m^{-2},[44] which is stronger than that of SiO/graphene. As a result, the initial energy barrier was higher, and a less nanomembrane was released after the same liquid treatment

(blue solid line in Figure 3d), which is also experimentally proved by the optical microscopy images. In contrast, low adhesion in SiO/graphene led to quicker delamination and a longer ΔL (red solid line in Figure 3d and marked in the inset image), highlighting the influence of adhesive interaction between the nanomembrane and their underlying substrate on delamination. It is proven that weak adhesion between graphene and versatile materials enables facile delamination of the nanomembranes from the substrate and the subsequent assembly of 3D microstructures.

Deterministic Fabrication of Tubular Microstructures on Graphene. We further explored the parallel integration of microtubes with different materials on the same piece of graphene, as sketched in Figure 4a. A hard mask was applied to define the desired deposition region. By rotation of the hard mask, nanomembranes were selectively deposited onto different regions and then released to form microtubes (Figure S15). The optical microscopy image elucidates successful fabrication of various microtubes, including a pure metal microtube and two hybrid microtubes, on the same graphene substrate. Moreover, the SEM image of the opening end of a SiO/Ti/Ni tube (inset of Figure 4a) suggests that the nanomembrane scrolls tightly and its surface is smooth and free of

contamination, benefiting from the smoothness of the deposition substrate.

Apart from the material issue, precise control of the rolling direction is desirable for determining the final structure of origami. A set of microtubes with rolling directions of 0, 45, 135, 180, 225, and 315° formed from circular nanomembranes are shown in Figure 4b. In this experiment, microdroplets are precisely placed in diverse positions of patterned nanomembranes with a micromanipulator, inducing release from the contact points. The circular nanomembrane tends to delaminate toward the direction perpendicular to the tangent of the contact point. Since the prestrained nanomembrane tends to relax along the direction with the fastest decrease in system potential energy,[45] which is dominated by the size of the released region, the delamination route is thus predetermined by nanomembrane geometry and the triggering point. More detailed records of the delamination procedure and the corresponding simulation results are depicted in Figure S16. Similar experiments were directed on rectangular (Figure S17), square, and parallelogram-shaped (Figure S18) nanomembranes. For parallelogram-shaped nanomembranes, triggering from the lower-left corner initiates scrolling toward the right. As the trigger point moves clockwise along the edge, the rolling direction follows, as shown in subsequent frames. Increasing the rolling diameter forms helical microstructures (Figure S19). In short, fabricated 3D microstructures possess various geometries, from microtubes to helical structures, mainly depending on the controlled rolling direction.

In addition to direction, controllable rolling diameter is also important for the accurate construction of 3D origami. As stated by the rolling mechanism, the curvature of the rolled-up microstructure is determined by the elastic property, built-in strain gradient, and nanomembrane thickness.[46] While the elastic property and built-in strain gradient originate from thermal and lattice mismatch that is influenced by multiple deposition factors (i.e., deposition rate in Figure S20) and material combinations (Figure S21),[17] nanomembrane thickness offers an opportunity to quantitatively tune the diameter of rolled-up structures,[46] as illustrated in Figure 4c. Here, circular patterns with diameters of 100 and 150 μm were chosen to eliminate geometric asymmetry that affects the total elastic energy, and nanomembranes were composed of SiO/Cr nanomembranes with thicknesses ranging from 20/20 to 60/60 nm. For each group, five microtubes were measured, and their statistic diameters were analyzed. It can be deduced that the rolling diameter increases with nanomembrane thickness, which is also supported by the optical microscopy images in the insets. As stated in Note S1, when the thicknesses of two layers remain equal, there exists a proportional relationship between the rolling diameter and the total nanomembrane thickness. Therefore, a linear fitting was employed, which matches well with the experimental results. On the other hand, the pattern size of the nanomembrane shows neglectable impact on the diameter of the microtube. Moreover, from the measured diameters, we obtained the precise value of built-in strain of SiO and Cr to be −0.519 and 0.401%, respectively (Note S3). We also characterized the built-in strain of the Si nanomembrane using Raman spectroscopy, which was then used as an input parameter for theoretical calculations of the microtube diameter. The resulting diameter of the corresponding Si/Ni microtube showed good agreement with the calculated values (details can be found in Note S3).

Deterministic Fabrication of Folding Structures.

Combining a controllable triggering process with a predesigned nanomembrane pattern, we further explore this nanomembrane-on-graphene strategy for more complicated folding origami. Typical folding structures contain two parts: two rigid plates and a hinge that connects them.[47] As the hinge deforms under a driving force, the orientation between two plates changes, and the whole structure transforms from planar to 3D architecture. A conceptual image of our folding structure is shown in Figure 5a. The multilayered nanomembrane with a built-in strain gradient contributes a proper driving force for bending of the hinge. For the construction of flat plates, we proposed a strain engineering strategy depicted in the left frame of Figure 5a. The plate consists of two groups of layers that possess the same contribution of materials with the same deposition parameters, only in a reversed order. As a result, the strain gradients in the two groups are equal in value while opposite in direction, and the neutralized strain gradient leads to the construction of a plane plate. Alternatively, the right frame of Figure 5a illustrates a side view of another rigid plate with a thick and hard layer of TiO₂ on top. This TiO₂ layer holds highly compressive strain, and its position slightly deviates from the underneath layer, forming a step-like structure that tightly locks the nanomembrane onto the graphene substrate, preventing the right plate from delamination and self-rolling. The left plate of the structure is then released from the substrate by a microdroplet, constructing a folding geometry. Optical microscopy images of the as-grown nanomembrane and folding structure after delamination are available in Figure S22.

For the deterministic formation of the folding structure, a simplified model was developed to investigate the geometry relationship between the folding angle θ, curvature diameter R, and hinge length L (Figure 5b). During stage I, where the plane panel rotates out of the plane and retains its freestanding morphology, the relationship can be calculated as $L = \pi R \theta / 180°$, according to the rolling essence of this folding mechanism. At this stage, R is determined by the inner strain gradient, and thus θ increases proportionally to L. In stage II where θ exceeds a critical point as the left plane panel touches the right layer locked on the substrate, R is further restricted by the requirement of a valid geometric structure, and the length of the flat panel a should be taken into consideration. An equation can be expressed as $\cos \theta = (R^2 - a^2)/(R^2 + a^2)$. Combined with the formula of hinge length L, the theoretical analysis of folding parameters is plotted in Figure 5c. Based on the theoretical results, we designed a series of patterns with altered L to demonstrate the capability of geometry control, and the SEM images of the triggered folding structures are shown in the first line in Figure 5d. As the L increases, θ increases accordingly, while R remains approximately the same. Finally, the panel reaches the nanomembrane surface, and the bending behavior is hindered, leading to a boost in the folding diameter that implies a stage II folding paradigm (the last column of Figure 5d). The angles and diameters of the experimental results are summarized and are in good agreement with theoretical results (Figure 5c). Moreover, we utilized the finite-element method (FEM) to simulate the folding process, and the results are shown in Figure 5c and the second line of Figure 5d, presenting good consistency between theoretical calculation/simulation and experimental results. The results also demonstrate the feasibility of our strategy for constructing complicated structures that require multiple
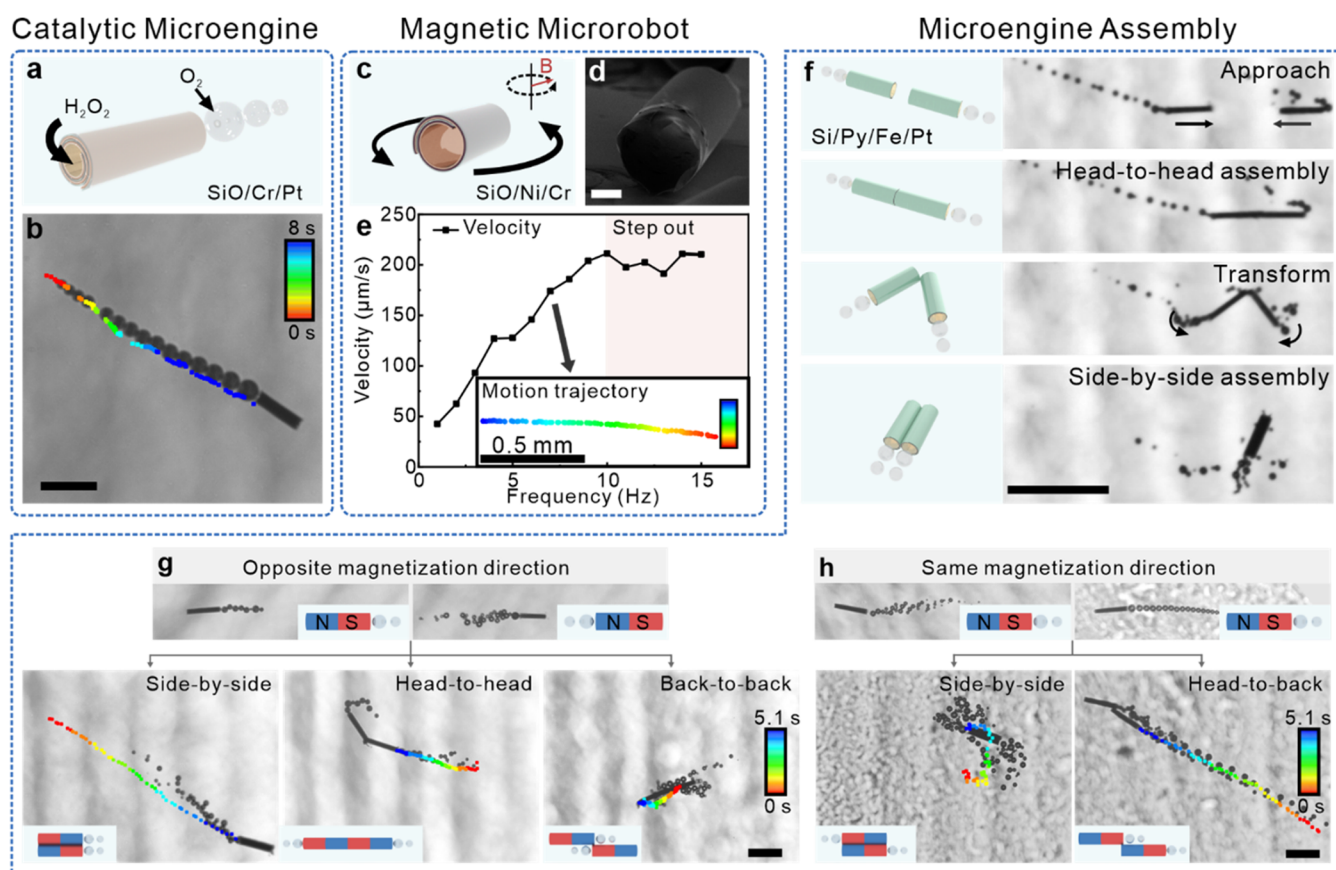
Figure 6. Application of functionalized rolled-up microstructures for catalytic and magnetic microrobot assembly. (a) Schematic of a rolled-up microtube consisting of SiO, Cr, and Pt functioning as a catalytic micromotor. (b) Optical microscopy image depicting the micromotor moving in 1% H_2O_2 solution. Colored dots illustrate the trajectory of the micromotor taken over 8 s. Scale bar, 100 μm. (c) Schematic of the magnetic microrobot consisting of SiO, Ni, and Cr. (d) SEM image of a single microtube on a graphene substrate. Scale bar, 10 μm. (e) Diagram of motion velocity as a function of rotation frequency of the magnetic field. The inset illustrates the trajectory of a microrobot in a magnetic field with a rotation frequency of 7 Hz. (f) Schematic illustration and optical images of two magnetic microrobot assembly under magnetic force and transformation into a different assembly pattern. Scale bar, 100 μm. (g) Schematic and the corresponding optical microscopy image of two micromotors with opposite magnetization directions and their three possible assembly patterns. Colored dots illustrate the trajectory of the micromotor assembly taken over 5.1 s. Scale bar, 100 μm. (h) Schematic and the corresponding optical microscopy image of two micromotors with the same magnetization direction and their two possible assembly patterns. Colored dots illustrate the trajectory of the micromotor assembly taken over 5.1 s. Scale bar, 100 μm.

fabrication steps, and a photolithography technique can be employed to fabricate more complex structures in the future (Figure S23).

Catalytic and Magnetic Microrobot Assembly. Owing to its material versatility and fabrication flexibility, our nanomembrane-on-graphene strategy forecasts its promising application in 3D microsystems. First, we demonstrate applications of assembled 3D origami by adding various functional layers during the fabrication process. In Figure 6a, a self-propelled micromotor was demonstrated by depositing an additional layer of 2 nm Pt onto SiO/Cr multilayers. After being triggered into a microtube, the inner side of the tube is covered with Pt which serves as a catalytic surface for hydrogen peroxide decomposition that produces oxygen. When the micromotor is transferred from the substrate into 2% H_2O_2 solution, oxygen gas bubbles were ejected out of the hollow structure of the micromotor which propels the micromotor to march forward. The motion trajectory follows a straight line (Figure 6b), and its velocity can be tuned by altering the length and diameter of the tubular structure through designing the nanomembrane thickness and the corresponding pattern's geometry. Another example presents a magnetic microrobot by

combining rolled-up origami with magnetic material (Figure 6c). As shown in the SEM image (Figure 6d), the microrobot consists of SiO, Ni, and Cr. The Ni layer functions as both the strain gradient layer and the magnetic actuation layer. By applying a rotating magnetic field, the robot rotates with a rotational axis parallel to that of the rotation magnetic field, actuating itself to proceed along a direction perpendicular to the rotational axis in a liquid environment. We chose the middle point of the tube to calculate its velocity, and the results are plotted in Figure 6e. The velocity increases with the increase of the rotation frequency before 10 Hz. When the frequency exceeds 10 Hz, the microrobot steps out, and the motion rate remains the same around 200 μm/s. To address the degradation issue in a liquid environment, further enhancements can be made by coating the micromotor with alumina using atomic layer deposition or by increasing the thickness of the outer layer to prolong the degradation time.

By combining the magnetic functional layer with a catalytic micromotor, we introduced a micromotor assembled by magnetic force. Figure 6f depicts the process of two micromotors (Si/Py/Fe/Pt) approaching and assembling in a 1% H_2O_2 solution. The two microtubes propel toward each
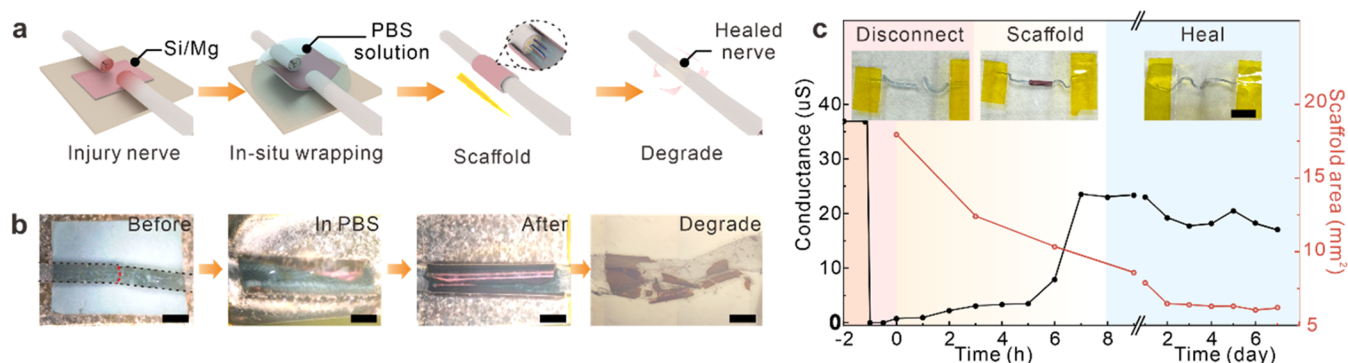
Figure 7. Application of the rolled-up microstructure as a nerve scaffold for peripheral nerve injury. (a) Illustration of the concept for in situ release of nanomembranes from graphene and subsequent wrapping around damaged nerves to promote healing. (b) Optical microscopy images of nanomembrane consisting of Si/Mg wrapped around a disconnected hydrogel for healing, which degraded after 7 days. The red dotted line marks the disconnected site of the hydrogel wire. Scale bar, 100 μm. (c) Healing process of hydrogel mimicking the healing of the injured nerve. The black line depicts the conductance of the hydrogel and the red line depicts the scaffolding area during the hydrogel healing process. Optical microscopy images show the healing process. Scale bar, 500 μm.

other (the first frame) until they encounter and assemble under the intrinsic magnetic force of the Py/Fe layer, forming a head-to-head assembly (the second frame). The external magnetic field can perturb the assembly, causing the two microtubes to rotate along the connection point (the third frame). This transformation process lasts for 0.6 s as the micromotors snapped into a side-by-side assembly pattern (the fourth frame). In fact, more assembly patterns can be observed in the experiment. As the head (solution inlet end) of the motor may have two possible magnetic poles, two kinds of micromotors can be produced: one with its magnetization direction in the direction of motion and the other with magnetization direction opposite to the direction of motion. Accordingly, there are two possible combinations of micromotor pairs, micromotors with the same magnetization direction and opposite magnetization direction, which form at least five possible assembly patterns in the experiment. Figure 6g depicts two micromotors with the same magnetization directions and their three possible assembly patterns, defined as the side-by-side, head-to-head, and back-to-back assembly. The speed of the side-by-side assembly is greater than that of each micromotor but slower than the sum of the two, as the micromotors are not propelled in exactly parallel directions due to minor geometric asymmetry. For the head-to-head and back-to-back pattern, the opposite propulsions lead to a slow motion in the solution. Similarly, Figure 6h depicts two micromotors with opposite magnetization directions and two possible assembly patterns. The side-by-side assembly exhibits a rotatory motion due to the fact that the vector of the propelling force does not pass through the center of the structure, while the head-to-head assembly moves quickly straightforward.

Conductive Nerve Scaffold. Leveraging the broad material selection and facile fabrication, we proposed another application of assembled 3D origami as a biodegradable scaffold for nerve repair. Peripheral nerve injury is a severe disease that can result in loss of sensory perception and motor function. In recent years, nerve scaffolds have been proposed for treating peripheral nerve injuries to facilitate nerve regeneration. Traditional nerve scaffolds require a complex surgical procedure to insert the injured nerve into a preformed conduit,[48] while our approach allows for the *in situ* wrapping of nanomembranes around the damaged nerve. As illustrated in

Figure 7a, the Si/Mg multilayer nanomembrane (both are biodegradable and biocompatible materials) on the graphene substrate is positioned beneath an injured nerve. The nanomembrane can be easily released in situ at the location of the damaged nerve using biocompatible liquids, such as PBS solution, directly wrapping around it to serve as a scaffold. This structure supports nerve regeneration by providing mechanical stability and delivering electrical signals, and it degrades naturally once healing is complete. As a proof of concept, a self-healing hydrogel with a relatively long healing time (12 h)[49] was chosen to mimic the healing process of the injured nerve (Figure 7b). The diameter of the hydrogel wire was approximately 1 mm, which is a typical diameter of peripheral nerves. The hydrogel wire was disconnected, and the two ends of the wire were placed on the 200/2000 nm thick Si/Mg multilayer (the first frame). A droplet of PBS solution was applied onto the nanomembrane, which immediately triggered the nanomembrane to delaminate and wrap around the hydrogel wire (the second frame), and the whole process lasted for only 80 s (Figure S24). After air-drying at room temperature, the broken hydrogel wire was fixed and can be suspended in air without fracture (the third frame). As a comparison, the ability of hydrogels with and without nerve scaffolds to withstand disturbance before complete self-healing was tested (Figure S25). When swayed in water, the hydrogel without the scaffold support disconnected again, while the scaffold-supported hydrogel maintained its structure, which demonstrates its mechanical support. The hydrogel then underwent a self-healing process, and the scaffold gradually degraded in PBS solution (the fourth frame). Figure 7c illustrates the changes in conductance during the hydrogel's severing, scaffolding, and healing processes. The conductance of the hydrogel was 37 μS when produced, which dropped to 0 μS when disconnected, 0.75 μS when scaffolded, and slowly increased to 23.6 μS after 7 h, demonstrating the healing of the hydrogel. Additionally, degradation of the scaffold during the healing process was characterized by monitoring the scaffold's area (Figure 7c), images of which are provided in Figure S26. After immersion in a 37 °C PBS solution for 12 h, the scaffold remained mostly intact. After 1 day, it began to fragment into several parts until it gradually peeled off and the remnant became transparent by the 7th day. The remaining nanomembrane was deduced to be silicon, which degraded much

slower than magnesium at a rate of approximately 4.5 nm/day at body temperature.[50] In the future, the performance of this nerve scaffold could be enhanced by adding a porous structure to the nanomembrane or coating it with factors that promote neuron growth.

CONCLUSIONS

In summary, we have demonstrated a nanomembrane-on-graphene strategy for nanomembrane delamination and 3D microstructure fabrication based on the unique surface characteristics of graphene. Energy analysis was applied to elucidate the dynamics of the liquid-triggered delamination process. Nanoindentation tests were conducted to prove the weak adhesion of various nanomembranes on graphene, and 3D origami of different materials were integrated on one piece of graphene. The rolling direction of nanomembranes can be determined by the microdroplet triggering point, and the diameter of microtubes was proved to be proportional to nanomembrane thickness, suggesting good control of the final assembled structure. By introducing a strain engineering strategy, a folding structure composed of panels and a hinge was constructed with the same release approach, and a geometry model was set up for predicting the folding angle, and FEM simulations match well with the resultant microstructures. Dry release strategies including roll-to-roll fabrication and thermal release were also achieved, which are more suitable for industrialized massive production. We utilized our nanomembrane-on-graphene strategy to construct chemically and magnetically driven micromotors, which can form micromotor assemblies with various motion behaviors. Finally, we demonstrated a conductive and biodegradable nerve scaffold that can be rapidly implanted onto a target injury point by a biocompatible solution. This work is expected to provide a convenient construction strategy for complex and multifunctional 3D microstructures for potential applications.

METHODS

Fabrication of Graphene. Monolayer graphene was grown on a Ge(110) wafer in a CVD system. The Ge substrate was placed in a quartz tube which was filled with H_2 of 30 sccm and Ar of 300 sccm and was heated up to 916 °C. After the temperature of the quartz tube reached 916 °C, the graphene growth process proceeded under a gas mixture of 2.2 sccm CH_4, 70.0 sccm H_2, and 700.0 sccm Ar. After deposition, the sample was cooled to room temperature.

Massive Production of Microtubes. The graphene substrate was covered by a shadow mask with circular pores. Then, the substrate was deposited with SiO (40 nm) and Cr (40 nm) through electron beam evaporation. The shadow mask was removed, and a drop of ethanol was dipped onto the sample surface.

Individual Release and Controllable Rolling of Nanomembranes. The graphene substrate was covered by a predesigned shadow mask. Then, the substrate was deposited with SiO (40 nm) and Cr (40 nm) through electron beam evaporation. After removing the shadow mask, a glass capillary containing ethanol contacts the edge of the patterned nanomembrane, and a microdroplet of ethanol was ejected onto the surface under capillary force. The position of the capillary tip was precisely controlled by a micromanipulator. Other multilayered structures were constructed by this method. The nanomembranes in Figure 1e are Cr/Ag/Ti/Fe (8/30/30/30 nm) for the circular pattern, SiO/Ni/Cr (30/30/30 nm) for the rectangular pattern, and SiO/Ni/Cr (30/40/30 nm) for the parallelogram pattern.

Roll-to-Roll Release. Monolayer graphene on copper foil (ZZ Standard; thickness = 35 μm) was used as the substrate for nanomembrane deposition. A shadow mask of circle patterns with a side length of 200 μm was covered onto the substrate, and Si/Ti/Ni (100/10/80 nm) was deposited. The sample was then wound around a roller.

Thermal Release. The nanomembranes consisting of Si, Ni, and Cr deposited on a graphene substrate were placed in a fast annealing oven and were heated to 400 °C for 480 s in a nitrogen atmosphere.

Nanoindentation. 40 nm Si nanomembrane, 40 nm SiO nanomembrane, and 40 nm Ag nanomembrane were individually deposited onto graphene, glass, Au, and Ge substrates for nanoindentation. A diamond tip was placed onto the sample, and the surface was scratched with an increasing load. The scratch load was slowly increased linearly from 0 to 50 mN during a scratching distance of 500 μm. The load−displacement data were analyzed to compare the adhesion properties.

Integration of Various Microtubes on One Graphene Chip. A shadow mask was covered onto the graphene substrate to define the shape of deposited nanomembranes. Then, electron beam evaporation was used to deposit Si/Ni/Cr (25/35/35 nm). After first deposition, the shadow mask was rotated 90° to choose the second area of the substrate, and SiO/Ti/Ni (25/35/40 nm) was deposited. The third deposition area was defined by the same method, and Cr/Ag/Ti/Fe (8/32/32/32 nm) was deposited. The shadow mask was then removed, and the nanomembranes were triggered by microdroplets.

Fabrication of the Folding Microstructure. A long rectangular patterned shadow mask was covered on the graphene substrate. SiO (40 nm), Cr (60 nm), and Ni (40 nm) were deposited onto the graphene substrate. Then, a second mask defined a short rectangular region on the left side of the as-deposited nanomembrane, followed by deposition of Ni (40 nm), Cr (60 nm), and SiO (40 nm). The third mask defined the region on the right side of the long rectangular region, and 100 nm TiO_2 was deposited. Then, the masks were removed, and the folding structure was triggered by a microdroplet.

Applications of Rolled-Up Microstructures. In the case of the catalytic micromotor, a circle-patterned nanomembrane consisting of SiO/Cr/Pt (40/40/2 nm) was deposited on graphene and released to form a tubular microstructure. The microtube was transported into a 1% hydrogen peroxide solution by a capillary tip. In the case of the magnetic microrobot, a rectangular shadow mask was applied, and SiO/Ni/Cr (40/60/40 nm) layers were grown and released. The microrobot was immersed in DI water in a trench on a glass slide. The motion trajectories were recorded by a CCD camera connected to an optical microscope. In the case of micromotor assembly, Si/Py/Fe/Pt (55/50/10/2 nm) layers were grown and released. In the case of nerve scaffold, a nanomembrane consisting of Si/Mg (200/2000 nm) was deposited on the graphene substrate. The hydrogel wire was disconnected and placed on the nanomembrane surface. Then, a drop of PBS solution was dipped onto the nanomembrane, which released the hydrogel wire.

ASSOCIATED CONTENT

ⓢ Supporting Information

The Supporting Information is available free of charge at https://pubs.acs.org/doi/10.1021/acsnano.4c07589.

Raman characterization of as-grown graphene; three stimulation methods; transfer process of nanomembrane and microtubes; an array of 35 × 20 nanomembranes by roll-to-roll strategy; graphene recycling; experimental setup for recording the delamination process; images of nanoindentation tests; images of tubes of different materials; comparison of release on different substrates; energy calculation of the delamination process; demonstration of thermal induced release; images of oxide microtubes, microtubes of fixed thickness, and folding structure; fabrication procedure of integrating versatile microtubes on graphene; images of directional delamination; Raman peak position of Si; illustration of the procedure to fabricate small-sized patterns that require

photolithography; photos of in situ wrapping; photos of the self-healing process with/without a scaffold; and notes for energy calculation and strain analysis (PDF)

AUTHOR INFORMATION

Corresponding Author

Yongfeng Mei − *Department of Materials Science & International Institute of Intelligent Nanorobots and Nanosystems, State Key Laboratory of Surface Physics and Shanghai Frontiers Science Research Base of Intelligent Optoelectronics and Perception, Institute of Optoelectronics, Fudan University, Shanghai 200438, People's Republic of China; Yiwu Research Institute of Fudan University, Yiwu 322000 Zhejiang, People's Republic of China;* orcid.org/0000-0002-3314-6108; Email: yfm@fudan.edu.cn

Authors

Yue Wu − *Department of Materials Science & International Institute of Intelligent Nanorobots and Nanosystems, State Key Laboratory of Surface Physics, Fudan University, Shanghai 200438, People's Republic of China; Yiwu Research Institute of Fudan University, Yiwu 322000 Zhejiang, People's Republic of China*

Xinyuan Zhang − *Department of Materials Science & International Institute of Intelligent Nanorobots and Nanosystems, State Key Laboratory of Surface Physics, Fudan University, Shanghai 200438, People's Republic of China*

Zhe Ma − *State Key Laboratory of Materials for Integrated Circuits, Shanghai Institute of Microsystem and Information Technology, Chinese Academy of Sciences, Shanghai 200050, People's Republic of China*

Weida Hong − *State Key Laboratory of Materials for Integrated Circuits, Shanghai Institute of Microsystem and Information Technology, Chinese Academy of Sciences, Shanghai 200050, People's Republic of China*

Chunyu You − *Department of Materials Science & International Institute of Intelligent Nanorobots and Nanosystems, State Key Laboratory of Surface Physics, Fudan University, Shanghai 200438, People's Republic of China; Yiwu Research Institute of Fudan University, Yiwu 322000 Zhejiang, People's Republic of China*

Hong Zhu − *Department of Materials Science & International Institute of Intelligent Nanorobots and Nanosystems, State Key Laboratory of Surface Physics, Fudan University, Shanghai 200438, People's Republic of China; Yiwu Research Institute of Fudan University, Yiwu 322000 Zhejiang, People's Republic of China*

Yang Zong − *Department of Materials Science & International Institute of Intelligent Nanorobots and Nanosystems, State Key Laboratory of Surface Physics, Fudan University, Shanghai 200438, People's Republic of China; Yiwu Research Institute of Fudan University, Yiwu 322000 Zhejiang, People's Republic of China*

Yuhang Hu − *Department of Materials Science & International Institute of Intelligent Nanorobots and Nanosystems, State Key Laboratory of Surface Physics, Fudan University, Shanghai 200438, People's Republic of China; Yiwu Research Institute of Fudan University, Yiwu 322000 Zhejiang, People's Republic of China*

Borui Xu − *Department of Materials Science & International Institute of Intelligent Nanorobots and Nanosystems, State Key Laboratory of Surface Physics, Fudan University, Shanghai 200438, People's Republic of China; Yiwu Research Institute of Fudan University, Yiwu 322000 Zhejiang, People's Republic of China;* orcid.org/0000-0001-5357-0400

Gaoshan Huang − *Department of Materials Science & International Institute of Intelligent Nanorobots and Nanosystems, State Key Laboratory of Surface Physics, Fudan University, Shanghai 200438, People's Republic of China; Yiwu Research Institute of Fudan University, Yiwu 322000 Zhejiang, People's Republic of China;* orcid.org/0000-0002-0525-7177

Zengfeng Di − *State Key Laboratory of Materials for Integrated Circuits, Shanghai Institute of Microsystem and Information Technology, Chinese Academy of Sciences, Shanghai 200050, People's Republic of China;* orcid.org/0000-0002-9357-5107

Complete contact information is available at:
https://pubs.acs.org/10.1021/acsnano.4c07589

Author Contributions

Conceptualization: Y.M. and B.X. Performing the experiments and theoretical analysis: Y.W. and X.Z. Fabrication of graphene: Z.M., W.H., and Z.D. Assistance in fabrication and characterization: C.Y., H.Z., Y.Z., and Y.H. Writing—original draft: Y.W. Writing—review and editing: Y.W., G.H., Z.D., and Y.M.

Notes

The authors declare no competing financial interest.

ACKNOWLEDGMENTS

REFERENCES

(1) Bhushan, B. Adhesion and Stiction: Mechanisms, Measurement Techniques, and Methods for Reduction. *J. Vac. Sci. Technol. B* **2003**, *21*, 2262.

(2) Kendall, K. Adhesion: Molecules and Mechanics. *Science* **1994**, *263*, 1720−1725.

(3) Eberhard, W.; Wcislo, W. Plenty of Room at the Bottom. *Am. Sci.* **2012**, *100*, 226.

(4) Maboudian, R.; Howe, R. T. Critical Review: Adhesion in Surface Micromechanical Structures. *J. Vac. Sci. Technol. B* **1997**, *15*, 1.

(5) Maboudian, R.; Carraro, C. Surface chemistry and tribology of MEMS. *Annu. Rev. Phys. Chem.* **2004**, *55*, 35−54.

(6) Huang, W.; Zhou, J.; Froeter, P. J.; Walsh, K.; Liu, S.; Kraman, M. D.; Li, M.; Michaels, J. A.; Sievers, D. J.; Gong, S.; Li, X. Three-Dimensional Radio-Frequency Transformers Based on a Self-Rolled-up Membrane Platform. *Nat. Electron.* **2018**, *1*, 305−313.

(7) Yu, X.; Huang, W.; Li, M.; Comberiate, T. M.; Gong, S.; Schutt-Aine, J. E.; Li, X. Ultra-Small, High-Frequency and Substrate-Immune Microtube Inductors Transformed from 2D to 3D. *Sci. Rep.* **2015**, *5*, No. 9661.

(8) Li, G.; Ma, Z.; You, C.; Huang, G.; Song, E.; Pan, R.; Zhu, H.; Xin, J.; Xu, B.; Lee, T.; An, Z.; Di, Z.; Mei, Y. F. Silicon Nanomembrane Phototransistor Flipped with Multifunctional Sensors toward Smart Digital Dust. *Sci. Adv.* **2020**, *6*, No. eaaz6511.

(9) Tian, Z.; Xu, B.; Wan, G.; Han, X.; Di, Z.; Chen, Z.; Mei, Y. F. Gaussian-Preserved, Non-Volatile Shape Morphing in Three-Dimensional Microstructures for Dual-Functional Electronic Devices. *Nat. Commun.* **2021**, *12*, No. 509.

(10) Fu, H.; Nan, K.; Bai, W.; Huang, W.; Bai, K.; Lu, L.; Zhou, C.; Liu, Y.; Liu, F.; Wang, J.; Han, M.; Yan, Z.; Luan, H.; Zhang, Y.; Zhang, Y.; Zhao, J.; Cheng, X.; Li, M.; Lee, J. W.; Liu, Y.; Fang, D.; Li, X.; Huang, Y.; Zhang, Y.; Rogers, J. A. Morphable 3D Mesostructures and Microelectronic Devices by Multistable Buckling Mechanics. *Nat. Mater.* **2018**, *17*, 268−276.

(11) Fang, H.; Zhao, J.; Yu, K. J.; Song, E.; Farimani, A. B.; Chiang, C.-H.; Jin, X.; Xue, Y.; Xu, D.; Du, W.; Seo, K. J.; Zhong, Y.; Yang, Z.; Won, S. M.; Fang, G.; Choi, S. W.; Chaudhuri, S.; Huang, Y.; Alam, M. A.; Viventi, J.; Aluru, N. R.; Rogers, J. A. Ultrathin, Transferred Layers of Thermally Grown Silicon Dioxide as Biofluid Barriers for Biointegrated Flexible Electronic Systems. *Proc. Natl. Acad. Sci. U.S.A.* **2016**, *113*, 11682−11687.

(12) Yan, Z.; Han, M.; Shi, Y.; Badea, A.; Yang, Y.; Kulkarni, A.; Hanson, E.; Kandel, M. E.; Wen, X.; Zhang, F.; Luo, Y.; Lin, Q.; Zhang, H.; Guo, X.; Huang, Y.; Nan, K.; Jia, S.; Oraham, A. W.; Mevis, M. B.; Lim, J.; Guo, X.; Gao, M.; Ryu, W.; Yu, K. J.; Nicolau, B. G.; Petronico, A.; Rubakhin, S. S.; Lou, J.; Ajayan, P. M.; Thornton, K.; Popescu, G.; Fang, D.; Sweedler, J. V.; Braun, P. V.; Zhang, H.; Nuzzo, R. G.; Huang, Y.; Zhang, Y.; Rogers, J. A. Three-Dimensional Mesostructures as High-Temperature Growth Templates, Electronic Cellular Scaffolds, and Self-Propelled Microrobots. *Proc. Natl. Acad. Sci. U.S.A.* **2017**, *114*, E9455−E9464.

(13) Li, X.; Wang, Y.; Xu, B.; Chen, Y.; Tian, Z.; Huang, G.; Mei, Y. F. Growth and Stress Analyses of Vanadium Dioxide Nanomembranes for Controllable Rolling. *J. Phys. D: Appl. Phys.* **2020**, *53*, No. 455105.

(14) Magdanz, V.; Medina-Sánchez, M.; Chen, Y.; Guix, M.; Schmidt, O. G. How to Improve Spermbot Performance. *Adv. Funct. Mater.* **2015**, *25*, 2763−2770.

(15) Bhat, K. N. Micromachining for Microelectromechanical Systems. *Def. Sci. J.* **1998**, *48*, 5−19.

(16) Auciello, O.; Birrell, J.; Carlisle, J. A.; Gerbi, J. E.; Xiao, X.; Peng, B.; Espinosa, H. D. Materials Science and Fabrication Processes for a New MEMS Technology Based on Ultrananocrystalline Diamond Thin Films. *J. Phys.: Condens. Matter* **2004**, *16*, R539−R552.

(17) Mei, Y. F.; Huang, G.; Solovev, A. A.; Ureña, E. B.; Mönch, I.; Ding, F.; Reindl, T.; Fu, R. K. Y.; Chu, P. K.; Schmidt, O. G. Versatile Approach for Integrative and Functionalized Tubes by Strain Engineering of Nanomembranes on Polymers. *Adv. Mater.* **2008**, *20*, 4085−4090.

(18) Li, X. Strain Induced Semiconductor Nanotubes: From Formation Process to Device Applications. *J. Phys. D: Appl. Phys.* **2008**, *41*, No. 193001.

(19) Huang, G.; Mei, Y. F. Assembly and Self-Assembly of Nanomembrane Materials-From 2D to 3D. *Small* **2018**, *14*, No. 1703665.

(20) Xu, C.; Wu, X.; Huang, G.; Mei, Y. F. Rolled-up Nanotechnology: Materials Issue and Geometry Capability. *Adv. Mater. Technol.* **2019**, *4*, No. 1800486.

(21) Liger, M.; Rodger, D. C.; Tai, Y.-C. In *Robust Parylene-to-Silicon Mechanical Anchoring*, The Sixteenth Annual International Conference on Micro Electro Mechanical Systems, 2003; pp 602−605.

(22) Estrine, E. C.; Robbins, W. P.; Maqableh, M. M.; Stadler, B. J. H. Electrodeposition and Characterization of Magnetostrictive Galfenol (FeGa) Thin Films for Use in Microelectromechanical Systems. *J. Appl. Phys.* **2013**, *113*, No. 17A937.

(23) Xu, B.; Zhang, X.; Tian, Z.; Han, D.; Fan, X.; Chen, Y.; Di, Z.; Qiu, T.; Mei, Y. F. Microdroplet-Guided Intercalation and Deterministic Delamination towards Intelligent Rolling Origami. *Nat. Commun.* **2019**, *10*, No. 5019.

(24) Cui, X.; Kong, Z.; Gao, E.; Huang, D.; Hao, Y.; Shen, H.; Di, C. A.; Xu, Z.; Zheng, J.; Zhu, D. Rolling up Transition Metal Dichalcogenide Nanoscrolls via One Drop of Ethanol. *Nat. Commun.* **2018**, *9*, No. 1301.

(25) Zhao, B.; Wan, Z.; Liu, Y.; Xu, J.; Yang, X.; Shen, D.; Zhang, Z.; Guo, C.; Qian, Q.; Li, J.; Wu, R.; Lin, Z.; Yan, X.; Li, B.; Zhang, Z.; Ma, H.; Li, B.; Chen, X.; Qiao, Y.; Shakir, I.; Almutairi, Z.; Wei, F.; Zhang, Y.; Pan, X.; Huang, Y.; Ping, Y.; Duan, X.; Duan, X. High-Order Superlattices by Rolling up van Der Waals Heterostructures. *Nature* **2021**, *591*, 385−390.

(26) Hammad, M.; Adjizian, J.-J.; Sacré, C.-H.; Huet, B.; Charlier, J.-C.; Raskin, J.-P.; Pardoen, T. Adhesionless and Near-Ideal Contact Behavior of Graphene on Cu Thin Film. *Carbon* **2017**, *122*, 446−450.

(27) Kim, J.; Bayram, C.; Park, H.; Cheng, C.-W.; Dimitrakopoulos, C.; Ott, J. A.; Reuter, K. B.; Bedell, S. W.; Sadana, D. K. Principle of Direct van Der Waals Epitaxy of Single-Crystalline Films on Epitaxial Graphene. *Nat. Commun.* **2014**, *5*, No. 4836.

(28) Alaskar, Y.; Arafin, S.; Lin, Q.; Wickramaratne, D.; McKay, J.; Norman, A. G.; Zhang, Z.; Yao, L.; Ding, F.; Zou, J.; Goorsky, M. S.; Lake, R. K.; Zurbuchen, M. A.; Wang, K. L. Theoretical and Experimental Study of Highly Textured GaAs on Silicon Using a Graphene Buffer Layer. *J. Cryst. Growth* **2015**, *425*, 268−273.

(29) Qiao, K.; Liu, Y.; Kim, C.; Molnar, R. J.; Osadchy, T.; Li, W.; Sun, X.; Li, H.; Myers-Ward, R. L.; Lee, D.; Subramanian, S.; Kim, H.; Lu, K.; Robinson, J. A.; Kong, W.; Kim, J. Graphene Buffer Layer on SiC as a Release Layer for High-Quality Freestanding Semiconductor Membranes. *Nano Lett.* **2021**, *21*, 4013−4020.

(30) Zhang, Z.; Xu, X.; Qiao, R.; Liu, J.; Feng, Y.; Zhang, Z.; Song, P.; Wu, M.; Zhu, L.; Yang, X.; Gao, P.; Liu, L.; Xiong, J.; Wang, E.; Liu, K. Low-Temperature Epitaxy of Transferable High-Quality Pd(111) Films on Hybrid Graphene/Cu(111) Substrate. *Nano Res.* **2019**, *12*, 2712−2717.

(31) Wu, J. B.; Lin, M. L.; Cong, X.; Liu, H. N.; Tan, P. H. Raman Spectroscopy of Graphene-Based Materials and Its Applications in Related Devices. *Chem. Soc. Rev.* **2018**, *47*, 1822−1873.

(32) Maugis, D. Subcritical Crack Growth, Surface Energy, Fracture Toughness, Stick-Slip and Embrittlement. *J. Mater. Sci.* **1985**, *20*, 3041−3073.

(33) Cao, Z.; Tao, L.; Akinwande, D.; Huang, R.; Liechti, K. M. Mixed-Mode Interactions between Graphene and Substrates by Blister Tests. *J. Appl. Mech.* **2015**, *82*, 081008.

(34) Ma, J.; Kim, J. M.; Hoque, M. J.; Thompson, K. J.; Nam, S.; Cahill, D. G.; Miljkovic, N. Role of Thin Film Adhesion on Capillary Peeling. *Nano Lett.* **2021**, *21*, 9983−9989.

(35) Akinwande, D.; Brennan, C. J.; Bunch, J. S.; Egberts, P.; Felts, J. R.; Gao, H.; Huang, R.; Kim, J. S.; Li, T.; Li, Y.; Liechti, K. M.; Lu, N.; Park, H. S.; Reed, E. J.; Wang, P.; Yakobson, B. I.; Zhang, T.; Zhang, Y. W.; Zhou, Y.; Zhu, Y. A Review on Mechanics and Mechanical Properties of 2D Materials—Graphene and Beyond. *Extreme Mech. Lett.* **2017**, *13*, 42−77.

(36) Gao, W.; Huang, R. Effect of Surface Roughness on Adhesion of Graphene Membranes. *J. Phys. D: Appl. Phys.* **2011**, *44*, No. 452001.

(37) He, Y.; Chen, W. F.; Yu, W. B.; Ouyang, G.; Yang, G. W. Anomalous Interface Adhesion of Graphene Membranes. *Sci. Rep.* **2013**, *3*, No. 2660.

(38) Boddeti, N. G.; Koenig, S. P.; Long, R.; Xiao, J.; Bunch, J. S.; Dunn, M. L. Mechanics of Adhered, Pressurized Graphene Blisters. *J. Appl. Mech.* **2013**, *80*, 040909.

(39) Koenig, S. P.; Boddeti, N. G.; Dunn, M. L.; Bunch, J. S. Ultrastrong Adhesion of Graphene Membranes. *Nat. Nanotechnol.* **2011**, *6*, 543−546.

(40) Li, J.; Zhang, J.; Gao, W.; Huang, G.; Di, Z.; Liu, R.; Wang, J.; Mei, Y. Dry-Released Nanotubes and Nanoengines by Particle-Assisted Rolling. *Adv. Mater.* **2013**, *25*, 3715−3721.

(41) Ugarte, D. Curling and Closure of Graphitic Networks under Electron-Beam Irradiation. *Nature* **1992**, *359*, 167−169.

(42) Qi, Y.; Wang, Y.; Pang, Z.; Dou, Z.; Wei, T.; Gao, P.; Zhang, S.; Xu, X.; Chang, Z.; Deng, B.; Chen, S.; Chen, Z.; Ci, H.; Wang, R.; Zhao, F.; Yan, J.; Yi, X.; Liu, K.; Peng, H.; Liu, Z.; Tong, L.; Zhang, J.; Wei, Y.; Li, J.; Liu, Z. Fast Growth of Strain-Free AlN on Graphene-Buffered Sapphire. *J. Am. Chem. Soc.* **2018**, *140*, 11935−11941.

(43) Anichini, C.; Samorì, P. Graphene-Based Hybrid Functional Materials. *Small* **2021**, *17*, No. 2100514.

(44) Kennedy, M. S.; Moody, N. R.; Adams, D. P.; Clift, M.; Bahr, D. F. Environmental Influence on Interface Interactions and Adhesion of Au/SiO2. *Mater. Sci. Eng. A* **2008**, *493*, 299−304.

(45) Cendula, P.; Kiravittaya, S.; Mönch, I.; Schumann, J.; Schmidt, O. G. Directional Roll-up of Nanomembranes Mediated by Wrinkling. *Nano Lett.* **2011**, *11*, 236−240.

(46) Nikishkov, G. P. Curvature Estimation for Multilayer Hinged Structures with Initial Strains. *J. Appl. Phys.* **2003**, *94*, 5333.

(47) Liu, Z.; Cui, A.; Li, J.; Gu, C. Folding 2D Structures into 3D Configurations at the Micro/Nanoscale: Principles, Techniques, and Applications. *Adv. Mater.* **2019**, *31*, 1802211.

(48) Apsite, I.; Constante, G.; Dulle, M.; Vogt, L.; Caspari, A.; Boccaccini, A. R. 4D Biofabrication of Fibrous Artificial Nerve Graft for Neuron Regeneration. *Biofabrication* **2020**, *12*, No. 035027.

(49) Caprioli, M.; Roppolo, I.; Magdassi, S.; et al. 3D-Printed Self-Healing Hydrogels via Digital Light Processing. *Nat. Commun.* **2021**, *12*, No. 2462.

(50) Hwang, S. W.; Park, G.; Edwards, C.; Corbin, E. A.; Kang, S. K.; Cheng, H.; Song, J. K.; Kim, J. H.; Yu, S.; Ng, J.; Lee, J. E.; Kim, J.; Yee, C.; Bhaduri, B.; Su, Y.; Omennetto, F. G.; Omennetto, F. G.; Huang, Y.; Huang, Y.; Bashir, R.; Bashir, R.; Goddard, L.; Goddard, L.; Popescu, G.; Popescu, G.; Lee, K. M.; Lee, K. M.; Rogers, J. A. Dissolution Chemistry and Biocompatibility of Single-Crystalline Silicon Nanomembranes and Associated Materials for Transient Electronics. *ACS Nano* **2014**, *8*, 5843−5851.